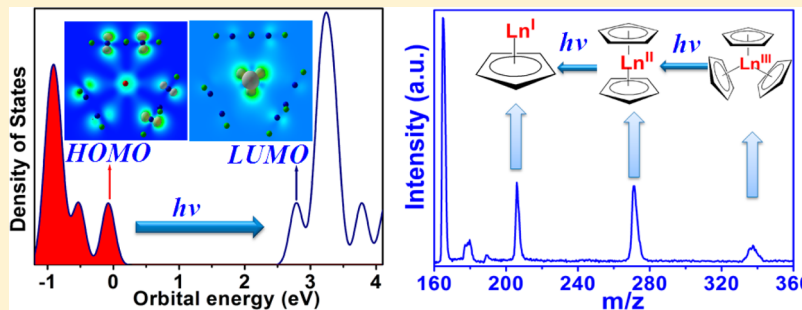


Photofragmentation of Gas-Phase Lanthanide Cyclopentadienyl Complexes: Experimental and Time-Dependent Excited-State Molecular Dynamics

Jiangchao Chen, Andrew M. Hochstatter, Dmitri Kilin, P. Stanley May, Qingguo Meng,* and Mary T. Berry*

Department of Chemistry, University of South Dakota, Vermillion, South Dakota 57069, United States

Supporting Information



ABSTRACT: Unimolecular gas-phase laser-photodissociation reaction mechanisms of open-shell lanthanide cyclopentadienyl complexes, $\text{Ln}(\text{Cp})_3$ and $\text{Ln}(\text{TMCp})_3$, are analyzed from experimental and computational perspectives. The most probable pathways for the photoreactions are inferred from photoionization time-of-flight mass spectrometry (PI-TOF-MS), which provides the sequence of reaction intermediates and the distribution of final products. Time-dependent excited-state molecular dynamics (TDESMD) calculations provide insight into the electronic mechanisms for the individual steps of the laser-driven photoreactions for $\text{Ln}(\text{Cp})_3$. Computational analysis correctly predicts several key reaction products as well as the observed branching between two reaction pathways: (1) ligand ejection and (2) ligand cracking. Simulations support our previous assertion that both reaction pathways are initiated via a ligand-to-metal charge-transfer (LMCT) process. For the more complex chemistry of the tetramethylcyclopentadienyl complexes $\text{Ln}(\text{TMCp})_3$, TMESMD is less tractable, but computational geometry optimization reveals the structures of intermediates deduced from PI-TOF-MS, including several classic “tuck-in” structures and products of Cp ring expansion. The results have important implications for metal–organic catalysis and laser-assisted metal–organic chemical vapor deposition (LCVD) of insulators with high dielectric constants.

INTRODUCTION

Lanthanide-containing materials, including the oxides, carbides, nitrides, and borides, have found wide applications in capacitors,¹ transistors,² light-emitting diodes,³ and superconductors⁴ due to their unique electrical, optical, and magnetic properties. The large band gaps in lanthanide oxides (e.g., 5.6 eV for Gd_2O_3) make them good insulators. High dielectric constants (e.g., $\kappa = 10$ for Gd_2O_3),⁵ large band gaps, symmetrical band offsets, and good thermodynamic stability⁶ suggest these materials as attractive candidates for the next generation of insulating gate oxides.⁷

The high-purity metal oxide films used in these applications are often deposited by metal–organic chemical vapor deposition (MOCVD) or atomic layer deposition (ALD), usually with postdeposition treatment or with use of an oxidizing coprecursor such as O_3 or H_2O . For example, lanthanide cyclopentadienyl complexes have been employed as ALD precursors for Er_2O_3 thin-film fabrication using H_2O as the oxidant.⁸ A constant growth rate of $\sim 1.5 \text{ \AA}$ per cycle was

observed, and the films, deposited at 250°C , contained <0.3 atom % of carbon impurities and <2.9 atom % of hydrogen impurities.

The cyclopentadienyl precursors are also potential candidates for laser-assisted metal–organic chemical vapor deposition (LCVD), which would allow the use of lower film-deposition temperature.⁹ However, the potential still remains for hydrocarbon contamination in the deposited films. In previous work, we^{10–12} and others^{13–15} have shown that photoionization time-of-flight mass spectrometry (PI-TOF-MS) is a useful tool for elucidating photofragmentation mechanisms in gas-phase MOCVD precursors, including processes giving rise to fluoride contamination from frequently used fluorinated precursors.

Here, we investigate the unimolecular photodissociation mechanisms for lanthanide-based cyclopentadienyl (Cp) and tetramethylcyclopentadienyl (TMCp) complexes from exper-

Received: September 25, 2013

Published: March 27, 2014

imental and computational perspectives. We propose the mechanisms whereby photolysis leads to either (1) clean stripping of the ligands from the metal or (2) ligand cracking within the ligand–metal complex. The latter process produces metal hydrocarbide compounds, which are a source of contamination in the production of high-purity metal and metal oxide films using CVD techniques. The most probable pathways for the photoreactions are inferred from photoionization time-of-flight mass spectrometry (PI-TOF-MS), which provides the sequence of reaction intermediates and the distribution of final products. DFT-based time-dependent excited-state molecular dynamics (TDESMD), in the case of $\text{Ln}(\text{Cp})_3$, and DFT-based reaction-intermediate geometry optimization, in the case of $\text{Ln}(\text{TMCP})_3$, is used to test the plausibility of the proposed reaction mechanisms and to provide insight into the electronic mechanisms for the individual steps of the laser-driven photoreactions. This powerful combination of experiment and theory has allowed an unprecedented level of certainty in the deduction of a mechanism for a very complex set of reactions.

■ EXPERIMENTAL SECTION

Tris(η^5 -cyclopentadienyl)lanthanide ($\text{Ln}(\text{Cp})_3$, $\text{Ln} = \text{La}, \text{Pr}, \text{Gd}$) and tris(tetramethylcyclopentadienyl)lanthanide ($\text{Ln}(\text{TMCP})_3$, $\text{Ln} = \text{Gd}, \text{Tb}$) precursors were purchased from Sigma-Aldrich and used as received. Photofragmentation experiments were conducted using a laser-photoionization time-of-flight mass spectrometer (PI-TOF-MS) described in detail in previous work.^{10,12} The cyclopentadienyl-type precursors are air and moisture sensitive and were loaded into the sample holder inside a controlled-atmosphere (Ar) glovebox. In contrast to our earlier work, no carrier gas was used. With no carrier gas, the pressure differential between the sample holder (10 mTorr) and the TOF chamber (10^{-4} mTorr) allows the precursor vapor to effuse into the TOF chamber. The sample holder was heated to sublime the precursors at 150–170 °C. Photofragmentation wavelengths of 266 nm (fourth harmonic of a Nd:YAG laser with 70 mJ pulse energies, $1.5 \times 10^9 \text{ W/cm}^2$) and 430 nm (Nd:YAG laser pumped optical parametric oscillator with 30 mJ pulse energies, $6.4 \times 10^8 \text{ W/cm}^2$) were used. Of the two photoionization sources, the YAG laser (Continuum Surelite) provided better resolution in the mass spectra because of the high-quality beam profile, whereas the optical parametric oscillator (Continuum, SLOPO) provided a stronger signal for the parent ion and for early intermediates in the fragmentation process.

Computational Method. The TDESMD methodology is described in detail in an earlier publication.¹⁶ Briefly, a tris(η^5 -cyclopentadienyl)lanthanum model, $\text{La}(\text{Cp})_3$, was built with three Cp rings η^5 -bonded to a central lanthanum ion. Geometry optimization, by minimization of the internal electronic energy, was performed using density functional theory (DFT) within the Vienna Ab initio Simulation Package (VASP) software.^{17–19} The simulation of the photofragmentation process of lanthanide precursors was investigated by periodic excitation of the $\text{La}(\text{Cp})_3$ model. In this method, a set of nuclear configurations at subsequent instants of time is calculated from the initial positions, and the generated trajectory is obtained through ab initio molecular dynamics for a time-dependent excited state: that is, time-dependent excited-state molecular dynamics (TDESMD). The one-electron Hamiltonian, $H_{ik}(t)$, and transition dipole, $\vec{\mu}_{ik}$, are expressed in the basis of Kohn–Sham orbitals. The one-electron Hamiltonian can be expressed as in eq 1 in relation to the Kohn–

$$H_{ik}(t) = H_{ik}^{\text{KS}}(t) - \vec{\mu}_{ik}(t) \cdot \vec{E}(t) \quad (1)$$

Sham Hamiltonian, $H_{ik}^{\text{KS}}(t)$, and the dipole interaction with the electric field, $\vec{E}(t)$. As a first approximation, the transition dipole is computed for the optimized initial geometry and treated as a constant throughout

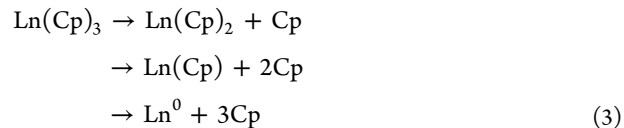
the trajectory. The Rabi frequency, Ω_{ik}^{R} , is given in eq 2, where the amplitude of the laser electric field, \vec{E}_0 , is considered constant.

$$\Omega_{ik}^{\text{R}} = \vec{\mu}_{ik} \cdot \vec{E}_0 \quad (2)$$

For the much larger $\text{La}(\text{TMCP})_3$ complexes, TDESMD was computationally intractable. However, DFT-based geometry optimization, performed separately for each of the intermediate masses determined by PI-TOF-MS, proved to be a valuable tool for determining intermediate structures and for testing hypotheses regarding mechanistic paths and branching along pathways.

■ RESULTS AND DISCUSSION

Tris(η^5 -cyclopentadienyl)lanthanide Precursors. Photoionization TOF Mass Spectra of $\text{Gd}(\text{Cp})_3$, $\text{Pr}(\text{Cp})_3$, and $\text{La}(\text{Cp})_3$. PI-TOF mass spectra for $\text{Gd}(\text{Cp})_3$, $\text{Pr}(\text{Cp})_3$, and $\text{La}(\text{Cp})_3$ are shown in Figure 1. The most prominent features observed in the low mass-to-charge (m/z) range of the PI-TOF mass spectra of $\text{Ln}(\text{Cp})_3$ are Ln^{2+} , Ln^+ , and LnC_2^+ . In the higher m/z range (>180 amu), additional Ln-containing species, including $\text{Ln}(\text{Cp})_3^+$, $\text{Ln}(\text{Cp})_2^+$, and $\text{Ln}(\text{Cp})^+$, are found. We have previously argued that a common theme in photofragmentation of gas-phase lanthanide complexes is ejection of intact neutral ligands through excitation of ligand-to-metal charge-transfer (LMCT) states.^{11,20} The spectra in Figure 1 support a similar mechanism for the $\text{Ln}(\text{Cp})_3$ complexes, according to



where Ln^0 is the neutral lanthanide metal. All of the species in this mechanism are neutral and are only observed in the mass spectrum when further photoionization captures the intermediates (e.g., $\text{Pr}(\text{Cp}) \rightarrow \text{Pr}(\text{Cp})^+ + e^-$) or the end product (e.g., $\text{Pr}^0 \rightarrow \text{Pr}^+ + e^- \rightarrow \text{Pr}^{2+} + 2e^-$). The ligand-stripping mechanism and subsequent product ionization is illustrated in Figure 1 with the parent, intermediates, and ultimate products for this reaction sequence shown in relation to the corresponding features in the mass spectrum.

However, this LMCT-mediated mechanism does not explain the presence of the LnC_2^+ fragment, featured strongly in Figure 1. The carbide is believed to be a product of a mechanism competing with intact ligand ejection: namely, the cracking of an attached ligand. This alternate reaction pathway is likely a principal source of carbon contamination in films deposited using $\text{Ln}(\text{Cp})_3$ precursors.

In Figure 1B, evidence for the Cp ligand cracking mechanism is seen in the PrC_3H_n^+ and PrC_4^+ fragments that appear between $\text{Pr}(\text{Cp})^+$ and PrC_2^+ . These fragments suggest that ligand cracking is a process competitive with ligand ejection for the $\text{Pr}(\text{Cp})$ complex. An analogous pattern is also seen in the photofragmentation of $\text{La}(\text{Cp})_3$ and $\text{Gd}(\text{Cp})_3$. In the latter case, it can be seen that at least some of the cracking chemistry occurs starting from $\text{Gd}(\text{Cp})_2$, which fragments to smaller molecules, such as $\text{Gd}(\text{Cp})(\text{C}_3\text{H}_3)$. Though the $\text{Ln}(\text{Cp})(\text{C}_3\text{H}_3)$ and $\text{Ln}(\text{Cp})(\text{C}_2\text{H})$ fragments are less apparent for $\text{Ln} = \text{Pr}, \text{La}$ than for the gadolinium analogues, a signal is still found for these components and they appear to be important intermediates in the fragmentation mechanism, as will be discussed below.

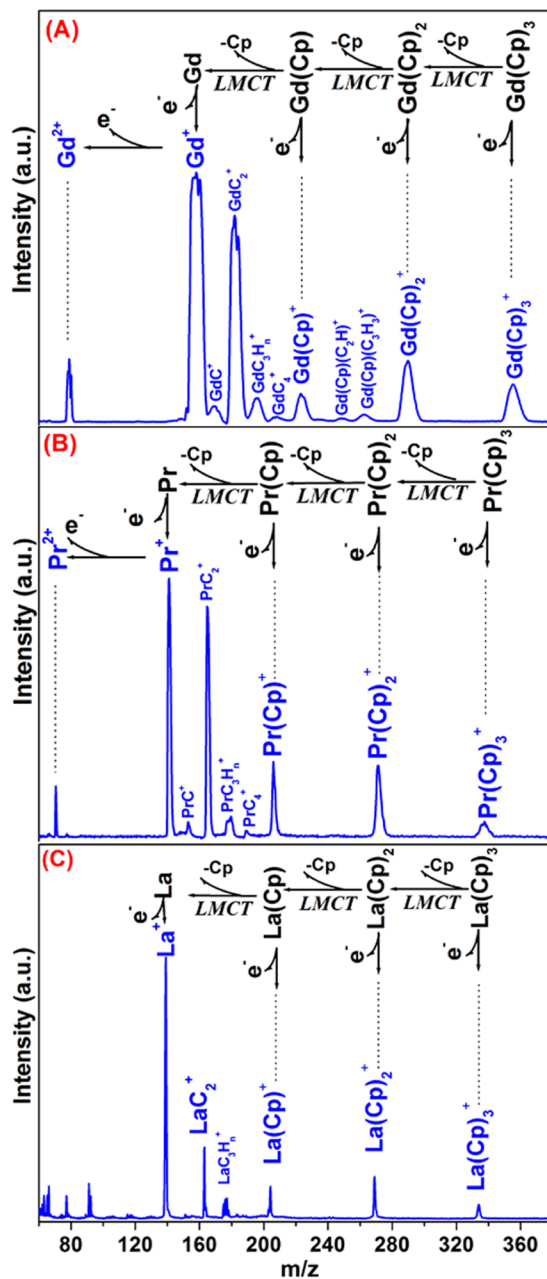


Figure 1. PI-TOF mass spectra of $\text{Gd}(\text{Cp})_3$ (A), $\text{Pr}(\text{Cp})_3$ (B), and $\text{La}(\text{Cp})_3$ (C) with photoexcitation at 430, 430, and 266 nm, respectively. The reaction diagram shows the photodissociation mechanism for LMCT stripping of the Cp ligand, and the subsequent photoionization of Ln^0 to Ln^+ and Ln^{2+} , in relation to the corresponding features in the mass spectrum. The illustrated reaction corresponds to line 1 in Scheme 1 and to eq 3 in the text.

Expanded portions of the mass spectra, relevant to the cracking chemistry, are shown in Figures 2 and 3. Important steps in the ligand-cracking mechanism and subsequent product ionization are also illustrated in Figures 2 and 3 and are related to the corresponding features in the mass spectrum. The $\text{Gd}(\text{Cp})_3$ spectra are somewhat complicated by the fact that there are five Gd isotopes with significant natural abundance. The assignment of GdC_3H_n ($n = 0-3$) features was confirmed by a simulated mass spectrum based on the natural abundance of the Gd isotopes and the branching ratio for the PrC_3H_n

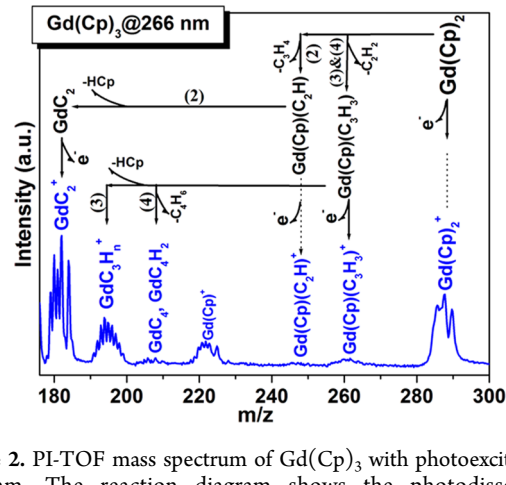


Figure 2. PI-TOF mass spectrum of $\text{Gd}(\text{Cp})_3$ with photoexcitation at 266 nm. The reaction diagram shows the photodissociation mechanism for cracking of the Cp ligand in relation to the corresponding features in the mass spectrum. The illustrated reaction corresponds to lines 2–4 in Scheme 1. Similar cracking is observed in $\text{La}(\text{Cp})_3$ and $\text{Pr}(\text{Cp})_3$.

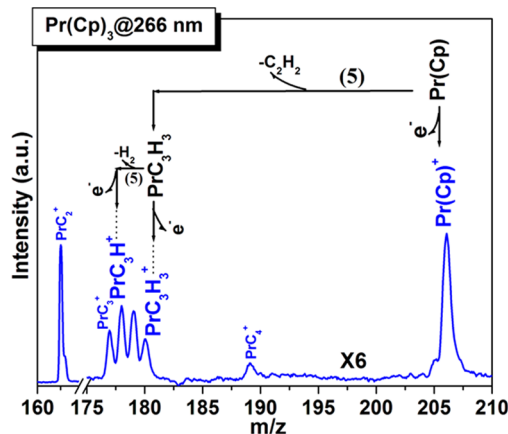


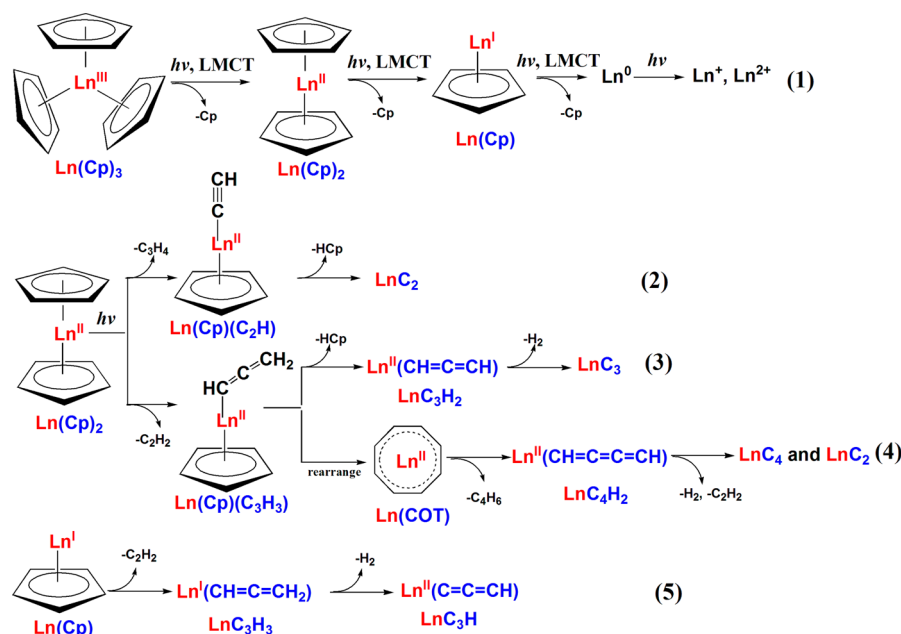
Figure 3. PI-TOF mass spectrum of $\text{Pr}(\text{Cp})_3$ with photoexcitation at 266 nm. The reaction diagram shows the photodissociation mechanism for cracking of the Cp ligand in relation to the corresponding features in the mass spectrum. The illustrated reaction corresponds to line 5 in Scheme 1. Similar cracking is observed in $\text{La}(\text{Cp})_3$ and $\text{Gd}(\text{Cp})_3$. An expanded region, comparing the LnC_3H_n and LnC_4H_n features for all three species, is given in the Supporting Information.

features, as shown in Figure 3. The GdC_3H_n simulation is included in the Supporting Information.

Photofragmentation Mechanism of $\text{Ln}(\text{Cp})_3$. For $\text{Ln}(\text{Cp})_3$, identification of the mass spectral features is fairly straightforward. Any mass higher than 71 amu, the mass of HCp , can most likely be attributed to a metal-containing fragment. For Gd, this can easily be confirmed by the isotopic signature. Subtracting the metal mass from the total mass of the fragment leaves a relatively small hydrocarbon mass and, generally, an unambiguous assignment of C_nH_m . Because of the stability of the cyclopentadienyl ring, C_5H_5 , $\text{C}_{10}\text{H}_{10}$, and $\text{C}_{15}\text{H}_{15}$ were confidently assigned to Cp , $(\text{Cp})_2$, and $(\text{Cp})_3$. Likewise C_8H_{5+n} was generally assigned to $(\text{Cp})(\text{C}_3\text{H}_n)$, C_7H_{5+n} was assigned to $(\text{Cp})(\text{C}_2\text{H}_n)$, etc. An important exception is C_8H_8 , which might be assigned to either $(\text{Cp})(\text{C}_3\text{H}_3)$ or to cyclooctatetraenyl dianion, COT^{2-} , as will be discussed further.

From the photofragments identified in Figures 1–3, the mechanisms for $\text{Ln}(\text{Cp})_3$ photofragmentation was deduced as

Scheme 1. Proposed Photofragmentation Mechanism for $\text{Ln}(\text{Cp})_3$ Showing Formation of Bare Metal in Line 1 as well as Formation of Carbon-Containing Fragments in Lines 2–5^a



^aThe oxidation state of the Ln ion is specified assuming the entire structure is neutral in charge.

illustrated in Scheme 1. The mechanism appears to be common to $\text{La}(\text{Cp})_3$, $\text{Pr}(\text{Cp})_3$, and $\text{Gd}(\text{Cp})_3$ and is illustrated generically for $\text{Ln}(\text{Cp})_3$. The photofragmentation of $\text{Ln}(\text{Cp})_3$ branches along one of two major pathways: (1) stepwise stripping of intact Cp ligands, corresponding to Scheme 1, line 1, and illustrated in Figure 1 and (2) cracking of bound Cp ligands, corresponding to Scheme 1, lines 2–5, and partially illustrated in Figures 2 and 3. The first major pathway leads to the production of bare lanthanide metal atoms, and the second major pathway leads to the production of lanthanide carbides. With regard to the notation used in Scheme 1, the formal oxidation state on the lanthanide is shown explicitly in most cases, but any charge is balanced by the organic fragment and the overall species are neutral. It should be noted that all of the chemistry we propose here involves neutral reactants and neutral fragments, which subsequently undergo photoionization to enable detection. This stands in contrast to typical 70 eV EI mass spectrometry, for which the ionization process creates high-energy ions which subsequently fragment.

Line 1 in Scheme 1 illustrates the LMCT-mediated stripping of intact Cp ligands, analogous to the previously proposed mechanism for $\text{Ln}(\text{thd})_3$, $\text{Ln}(\text{hfac})_3$, and $\text{Ln}(\text{fod})_3$.^{10,20} The suggested pathways for the ligand cracking in the $\text{Ln}(\text{Cp})_2$ complex, which lead ultimately to LnC_2 , LnC_3 , and LnC_4 , are shown in lines 2–4. The first step in $\text{Ln}(\text{Cp})_2$ cracking is the elimination of stable, closed-shell acetylene (C_2H_2) or propyne (C_3H_4) species to produce $\text{Ln}(\text{Cp})(\text{C}_3\text{H}_3)$ or $\text{Ln}(\text{Cp})(\text{C}_2\text{H})$ intermediates, respectively. The existence of these intermediates is supported by the $\text{Gd}(\text{Cp})(\text{C}_3\text{H}_3)^+$ and $\text{Gd}(\text{Cp})(\text{C}_2\text{H})^+$ features in the mass spectrum (Figures 1 and 2). Acetylene elimination from the gas-phase Cp radical has been widely reported in the literature,^{21–25} and the product of acetylene elimination, $\text{Gd}(\text{Cp})(\text{C}_3\text{H}_3)$, is more strongly represented than the product of propyne elimination, $\text{Gd}(\text{Cp})(\text{C}_2\text{H})$, in the mass spectra in Figure 2. Hydrogen is expected to be highly migratory within the excited complexes, and both $\text{Ln}(\text{Cp})$ -

(C_2H) and $\text{Ln}(\text{Cp})(\text{C}_3\text{H}_3)$ might be expected to eliminate HCp , producing LnC_2 and $\text{Ln}(\text{C}_3\text{H}_2)$, respectively (lines 2 and 3), the ions of which are observed prominently in the mass spectra for both $\text{Gd}(\text{Cp})_3$ and $\text{Pr}(\text{Cp})_3$. Subsequent elimination of H_2 from $\text{Ln}(\text{C}_3\text{H}_2)$ produces the observed LnC_3 species, as illustrated in line 3 of Scheme 1.

Referring to line 4 of Scheme 1, we suggest that an alternate decomposition pathway for the $\text{Ln}(\text{Cp})(\text{C}_3\text{H}_3)$ complex is responsible for the production of LnC_4 , which is observed as a weak feature in the mass spectrum. Here, LnC_4 is produced by reaction of the Cp group with C_3H_3 in the $\text{Ln}(\text{Cp})(\text{C}_3\text{H}_3)$ complex, eliminating stable butadiene, C_4H_6 , and leaving $\text{Ln}(\text{C}_4\text{H}_2)$, which subsequently eliminates H_2 or C_2H_2 to form the observed LnC_4 or LnC_2 fragments. It is likely that this fragmentation to LnC_4 proceeds through rearrangement of $\text{Ln}(\text{Cp})(\text{C}_3\text{H}_3)$ to the cyclooctatetraene complex, $\text{Ln}(\text{COT})$. Calculation shows the latter to be more stable by about 1 eV, and computed trajectories (see the Supporting Information) show a propensity for $\text{La}(\text{COT})$ to dissociate into the observed $\text{LaC}_4\text{H}_n + \text{C}_4\text{H}_m$ fragments.

The ions corresponding to all of the species described above were observed in the PL-TOF mass spectra (Figures 1–3). However, one feature, LnC_3H , observed fairly prominently in the mass spectrum, is not accounted for in the discussion above. We suggest that LnC_3H is produced via the cracking of LnCp following the pathway outlined in Figure 3 and in Scheme 1, line 5. In this case, LnCp eliminates C_2H_2 , leaving LnC_3H_3 , analogous to the first step in lines 3 and 4 and well-supported in the literature as a fragmentation path for the cyclopentadienyl radical.^{21–25} The LnC_3H_3 intermediate may also arise from the $\text{Ln}(\text{Cp})(\text{C}_3\text{H}_3)$ in line 4 following LMCT elimination of Cp. Elimination of H_2 from $\text{Ln}(\text{C}_3\text{H}_3)$ then results in the observed LnC_3H feature.

A generalized, conceptual explanation of the photofragmentation pathways illustrated in Scheme 1 is as follows. Excitation into the LMCT state creates molecular geometries that lie on a

repulsive wall of the LMCT state, well above the binding energy, where the repulsive force is in the direction of increased metal–ligand distance. Thus, LMCT excitation results in efficient (immediate) ejection of the intact Cp radical from the reduced metal. This is illustrated in line 1 of Scheme 1. Alternatively, if the energy of the excited state has the time and opportunity to redistribute into other degrees of freedom (as opposed to the metal–ligand dissociation trajectory), ligand cracking may be observed. Cracking, which proceeds at a more leisurely pace, follows a path of minimized potential energy, and all of the eliminated species are stable closed-shell molecules, such as acetylene, propyne, and molecular hydrogen.

The suggested relative time scales for these two types of processes are consistent with the simulations discussed below. If the ligand ejection is “immediate” upon excitation to the repulsive wall of the charge-transfer state, the clean ligand dissociation would be expected to occur on the time scale of one metal–ligand vibrational period (50–100 fs). The cracking dynamics, however, result from intramolecular vibrational redistribution (IVR) as energy from the compressed metal–ligand bond is redistributed into other degrees of freedom that result in the chemistry we observe. This might be expected to require several vibrational periods (hundreds of femtoseconds), and the dynamics might be expected to follow a much more tortuous path along the potential energy surface.

A fundamental hypothesis is that much, if not all, of the cracking chemistry, as discussed above, begins with the Cp radical, created through the LMCT transition. The Cp radical either fragments or, alternatively, extracts atoms from an adjacent Cp. A stable, closed-shell molecule is then ejected, and the retained radical fragment receives an electron back from the metal through a metal-to-ligand charge transfer (MLCT) process, forming an anion in a stable, or at least metastable, complex. For example, in line 5 of Scheme 1, $\text{Ln}(\text{Cp})$, or $\text{Ln}^+(\text{Cp}^-)$, produces a Cp^\bullet radical through LMCT, leading to $\text{Ln}^0(\text{Cp}^\bullet)$. The Cp^\bullet radical then fragments according to $\text{Ln}^0(\text{Cp}^\bullet) \rightarrow \text{Ln}^0(\text{C}_3\text{H}_3^\bullet) + \text{C}_2\text{H}_2$, ejecting a stable, closed-shell C_2H_2 molecule. The retained $\text{C}_3\text{H}_3^\bullet$ radical fragment receives an electron back from Ln^0 through an MLCT process, forming the $\text{Ln}^+(\text{C}_3\text{H}_3^-)$ product, which is detected by the PTOF mass spectrometer after further photoionization to the $[\text{Ln}^{2+}(\text{C}_3\text{H}_3^-)]^+$ ion, or, more simply, $\text{Ln}(\text{C}_3\text{H}_3)^+$.

Structures and reactions parallel to those proposed here have been reported in the literature. For example, acetylene elimination in the decomposition of cyclopentadienyl to produce propargyl has been widely reported.^{21–25} HCP elimination, proposed at several points in our photofragmentation mechanism, was reported in the surface reaction of ALD-grown Y_2O_3 on the Si-OH surface using $\text{Y}(\text{Cp})_3$ as the metal precursor.²⁶ Structures similar to $\text{Ln}(\text{Cp})(\text{C}_3\text{H}_3)$ and $\text{Ln}(\text{C}_3\text{H}_3)$ have been identified in other work. For example, $\text{Cr}(\text{Cp})(\text{C}_3\text{H}_3)$ and $\text{Cr}(\text{C}_3\text{H}_3)$ have been reported as stable fragments in the gas-phase laser photochemistry of chromocene.²⁷ Also, a stable YC_3H_3 product has been observed by Davis et al.²⁸ in the reaction of yttrium with 2-butyne. The formation and stability of small lanthanide carbides or metallocarbon clusters (LnC_n) have also been reported.²⁹ Carbyne structures with $\text{Ln}^{2+}-(\eta^2-\text{C}\equiv\text{C}^-)$ and $\text{Ln}^{2+}-(\eta^2-\text{C}\equiv\text{C}-\text{C}\equiv\text{C}^-)$ have been proposed for LnC_2 and LnC_4 clusters in which the Ln^{2+} ion is coordinated to both terminal carbons.³⁰ Our calculations for the minimum energy geometry for LnC_2 and LnC_4 are consistent with those proposed structures.

Ab Initio Simulation of Photodissociation of $\text{La}(\text{Cp})_3$ Precursor. Computational Model for $\text{Ln}(\text{Cp})_3$ Photofragmentation. The computational modeling of these dissociative photoreactions faces several key challenges in dealing explicitly with (i) high angular momentum 4f orbitals, (ii) excited-state geometries, (iii) reaction branching, and (iv) essentially nonstationary electronic states of the system. Here, f electrons are treated explicitly, while core electrons are described using appropriate pseudopotentials.

Since, for the present system, calculation of the multiple multidimensional potential energy surfaces (PESs) makes an impractically large computational demand, we have selected the time-dependent excited-state molecular dynamics (TDESMD) method, where the model “explores” the most probable nuclear configurations, forming a trajectory in phase space.^{16,31} The trajectory starts at a nuclear configuration representing the reactant and ends at nuclear configurations representing products.³² During the trajectory, the system is continually subjected to perturbation by the laser field and cycles between the ground and excited states at the inverse Rabi frequency, $\Omega_R^{-1} = 10$ fs, with time increments for simulation of 1 fs.

Computational Characterization of the Initial Reactant. The tris(cyclopentadienyl)lanthanum geometry-optimized model of $\text{La}(\text{Cp})_3$ is shown in Figure 4. This was used as the

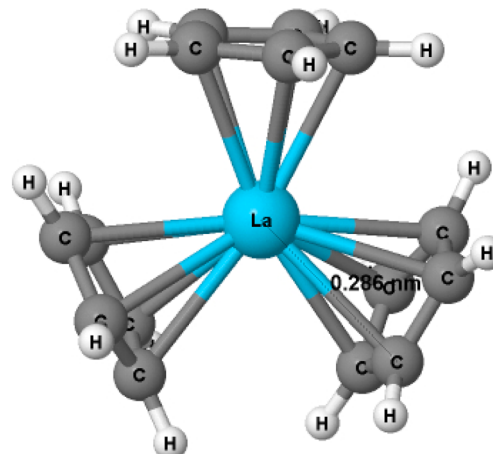


Figure 4. $\text{La}(\text{Cp})_3$ model used as the starting point in TDESMD simulations.

starting point for the TDESMD simulation described below. Analysis of the electronic structure of the unperturbed $\text{La}(\text{Cp})_3$ precursor is shown in Figure 5, with the most important pairs of occupied and unoccupied orbitals, those involved in strong optical transitions, shown in the Supporting Information. In the density of states (DOS) trace, positions labeled as Figure 5a–h indicate the energy positions of groups of one-electron orbitals. Selected Kohn–Sham orbitals corresponding to the labeled positions are illustrated by isosurfaces of partial charge density with colored spheres representing nuclear centers for La (red), H (green), and C (blue). In this illustration, LU designates the lowest unoccupied molecular orbital and LU+n designates the nth orbital above LU in energy. Likewise, HO designates the highest occupied molecular orbital and HO-n designates orbitals below HO in energy. In the DOS trace, feature a represents orbitals of p character delocalized over several carbons. Features b, c, d, g, and h show hybridization between the La^{3+} ion and the organic shell. Features e and f show compositions of seven orbitals with f character, approximately

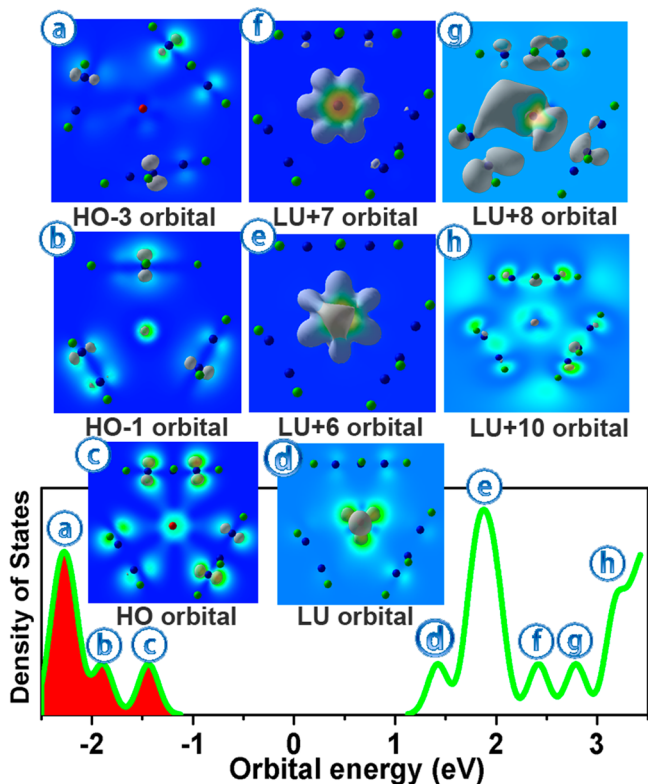


Figure 5. Density of states (DOS) for the unperturbed $\text{La}(\text{Cp})_3$ precursor computed by ground state DFT (green line). The red filled area in the DOS corresponds to occupied orbitals. One of the corresponding Kohn–Sham orbitals is selected from each group in the DOS for illustration. Each orbital is labeled using HOMO–LUMO notation and represented by isosurfaces (gray) of partial charge density with color spheres representing La (red), H (green), and C (blue).

corresponding to the seven different projections of orbital angular momentum. Thus, the optical transitions encompassed in Figure 5a–e have nearly pure ligand-to-metal charge-transfer

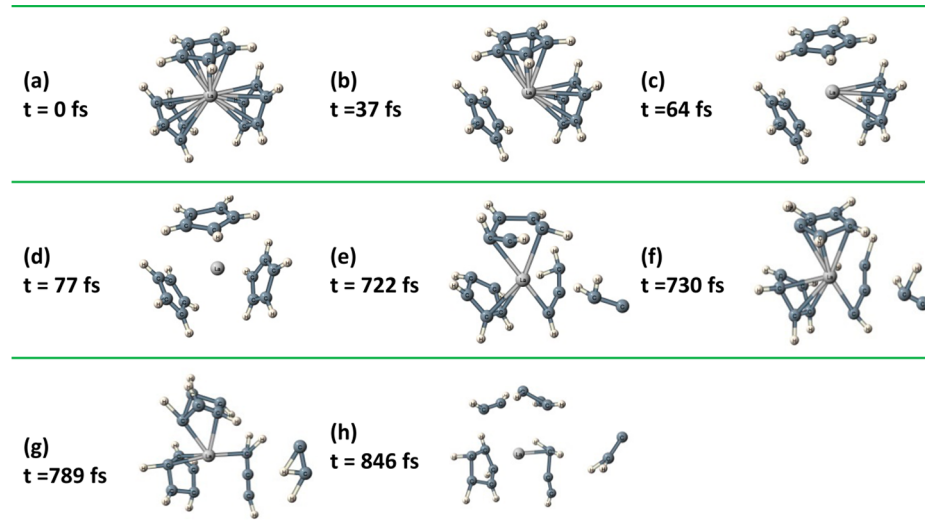
(LMCT) character and are calculated to have high oscillator strengths.

Time-Dependent Excited-State Molecular Dynamics Simulation of the Photodissociation of $\text{La}(\text{Cp})_3$. To simulate the photofragmentation of $\text{La}(\text{Cp})_3$ by the laser during the laser-assisted MOCVD process, we investigated how periodic excitation affects the electronic structure and nuclear configuration of the initial $\text{La}(\text{Cp})_3$ model. The initial nuclear configuration of the model is given by initial positions of each atom $\{\vec{R}_i(t=0)\}$. The ultimate goal is to find a nuclear trajectory, that is, a set of nuclear configurations at subsequent instants of time $\{\vec{R}_i(t)\}$, that leads from reactant to products. The trajectory is obtained through TDESMD for a time-dependent excited state.

For a given nuclear configuration, $\{\vec{R}_i\}$, the electronic structure was calculated as described previously.¹⁶ We then modified the occupation of electronic states according to the Rabi solution of the optical Bloch equation.^{33,34} The modified occupation was used to recompute the total electron density and internuclear forces. With new forces, an infinitesimal (1 fs) increment of atomic positions was computed. For an additional four 1 fs time intervals, the total electron density, internuclear forces, and atomic positions were recomputed. After these five increments in position, the occupation was returned to represent the ground electronic state of the new nuclear configuration, and five new increments in position were calculated. The computational procedure was repeated in an iterative way. Computation at each time interval generated a snapshot of the nuclear trajectory, which was analyzed for forming or breaking of specific chemical bonds. At later stages of the laser-driven molecular dynamics, bond breaking was observed, leading to breaking of the original molecular model into various fragments, which were compared with the experimental observation of fragments created by laser-induced photodecomposition.

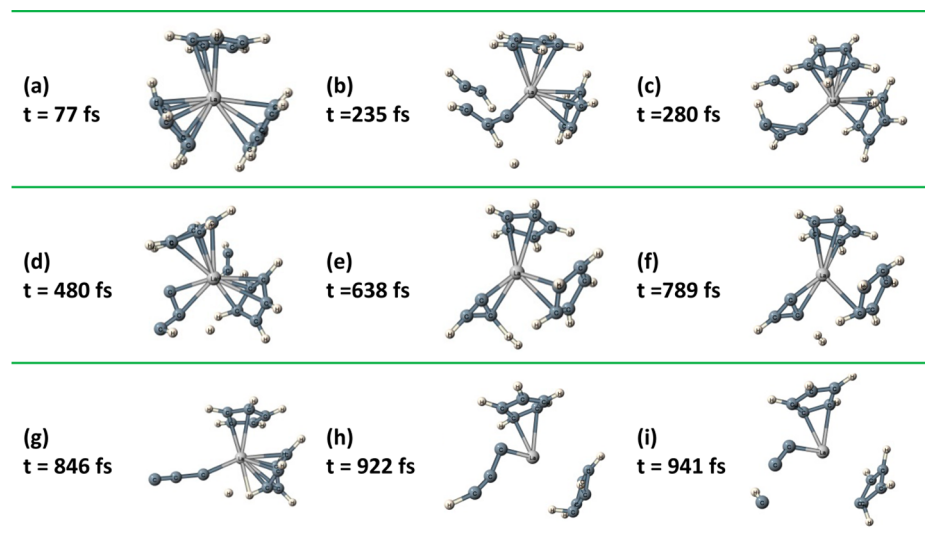
In Table 1, snapshots are given for the computed trajectory of $\text{La}(\text{Cp})_3$ driven by a laser field with Rabi oscillations at an initial excitation energy of $\hbar\Omega \approx \epsilon_{ij} = 5.40$ eV between orbitals $i = \text{HO-3}$ and $j = \text{LU+10}$ with an inverse Rabi frequency $\Omega_R^{-1} = 10$ fs^a

Table 1. Snapshots of the Computed Trajectory of $\text{La}(\text{Cp})_3$ Driven by the Laser Field in a Rabi Cycle between Orbitals $i = \text{HO-3}$ and $j = \text{LU+10}$ at an Excitation Energy of $\hbar\Omega \approx \epsilon_{ij} = 5.40$ eV with the Inverse Rabi Frequency $\Omega_R^{-1} = 10$ fs^a



^aStarting from $t = 0$ fs, eight snapshots along the trajectory are presented, corresponding to the specified time in femtoseconds.

Table 2. Snapshots of the Computed Trajectory of $\text{La}(\text{Cp})_3$ Driven by the Laser Field in a Rabi Cycle between $i = \text{HO-1}$ and $j = \text{LU}$ at an Excitation Energy of $\hbar\Omega \approx \epsilon_{ij} = 3.31$ eV with the Inverse Rabi Frequency $\Omega_R^{-1} = 10$ fs^a



^aStarting from $t = 77$ fs, nine snapshots are presented.

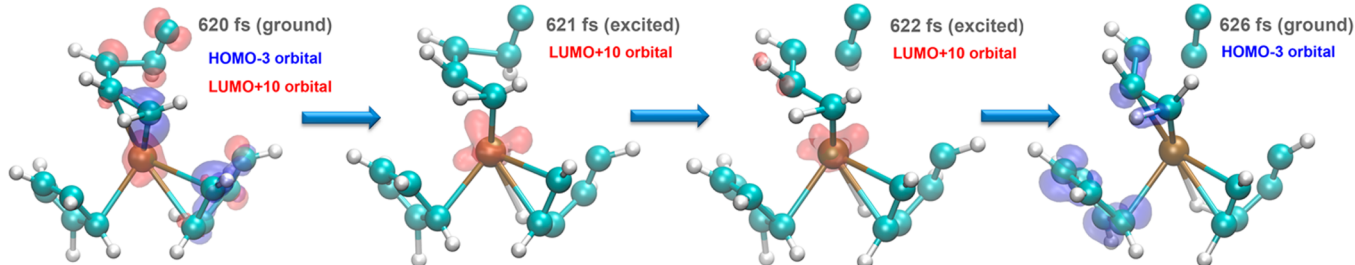


Figure 6. Partial charge density images from 620 to 626 fs for the trajectory shown in Table 1. The isosurface in blue is for the lower, HO-3 orbital, and the surface in red is for the excited, LU+10 orbital. Excitation from HO-3 to LU+10 results in charge transfer from the ligand anion to the metal at 620 fs. The charge-deficient ligand (nominally a neutral radical) cracks, ejecting a two-carbon fragment. The retained ligand fragment receives electron density back from the metal at 625 fs, stabilized in its attraction to the metal through strong Coulombic forces.

10 fs. The duration of simulation, t_{\max} , is 1000 fs. Whether atoms are shown as bound or not bound is determined by the interatomic distance. Between 0 and 77 fs, the ligands are sequentially ejected (shown as not bound) from the metal, consistent with the mechanism in line 1 of Scheme 1. However, as an artifact of the simulation model, the ligands are never lost entirely, since cycling to the ground state creates attractive Coulombic forces which recapture the ligand. Only repulsion and subsequent attraction of the ligands are observed for the first several hundred femtoseconds. At approximately 600 fs, one of the recaptured ligands begins to undergo cracking, and at 722 fs an acetylene molecule is eliminated, with the complex retaining the C_3H_3 portion of Cp. This is consistent with the chemistry proposed in the first steps of lines 4 and 5 in Scheme 1. The remaining trajectory predicts the facile migration of H atoms (722 to 789 fs) and the fragmentation of a second Cp into C_2H_2 and C_3H_3 (846 fs).

It should be noted that Table 1 illustrates the results of a single trajectory, whereas the laboratory photofragmentation experiment detects the results of many trajectories. No single trajectory will reproduce all of the observed fragments. The simulation parameters ϵ_{ij} and Ω_R may also be tuned to explore different trajectories. A second trajectory was run with ϵ_{ij} corresponding to the energy between orbitals $i = \text{HO-1}$ and $j = \text{LU}$, the snapshots of which are presented in Table 2. At 235

fs, we observe again the ejection of a neutral C_2H_2 . Simultaneously, the retained C_3H_3 is seen to transfer one hydrogen atom to a neighboring Cp, forming bound HCp and C_3H_2 at 280 fs. This is analogous to the first and second steps in line 3 of Scheme 1. However, in this simulation the HCp is not released and the hydrogen is transferred back to the C_3H_2 moiety. It seems likely that, with longer simulation times and multiple transfers of the hydrogen back and forth, the neutral HCp would eventually escape to a sufficient distance to prevent back transfer and the second step in line 3 might be accomplished. At the very least, the model supports the plausibility of the proposed hydrogen transfer from bound C_3H_3 to bound Cp. At 789 fs, the elimination of H_2 from bound C_3H_3 is observed, consistent with the last step in line 5 of Scheme 1. At 846, 922, and 941 fs, the precursors to the LnC_3 , LnC_3H , and LnC_2 fragments are also observed, albeit with other Cp rings still retained in the complex.

Simulation using rapid Rabi cycling does not allow the same degree of intramolecular redistribution of energy along the trajectory as we propose in our mechanism and the intermediate structures generally have not been allowed to relax to minimum energy geometries. Nevertheless, many of the features that we propose as plausible steps in the fragmentation are reproduced in the quantum simulation.

Electron Flow and Partial Charge Density Maps. The role played by the LMCT states and MLCT processes in the Cp cracking reactions can be seen clearly by following the charge density on the La(Cp)₃ complex during the reaction. Figure 6 shows snapshots of the partial charge density on the La(Cp)₃ complex within the 620–626 fs time window of the reaction trajectory illustrated in Table 1. The first structure in Figure 6 (*t* = 620 fs) illustrates the electron redistribution associated with a ligand-to-metal charge transfer transition, as represented by the promotion of an electron from HO-3 (blue orbital) to LU+10 (red orbital). The second and third structures of Figure 6 follow the propagation of the trajectory in the excited state. The second structure in Figure 6 (*t* = 621 fs) shows increased migration of charge in LU+10 from the Cp ligand to the La, with a net result of reduction of the metal and oxidation of the ligand. The third snapshot in Figure 6 (*t* = 622 fs) shows the elimination of a C₂H fragment from the excited Cp ligand. The last snapshot in Figure 6 (*t* = 626 fs) shows the return of electron density from the temporarily reduced metal to the still-bound portion of the ligand following the return of the complex to the ground state (i.e., the return of the electron from LU+10 to HO-3). We note that the two-carbon moiety does not permanently escape during this one Rabi cycle and 10 additional cycles of ligand-to-metal and metal-to-ligand charge transfer occur before the stable closed-shell C₂H₂ fragment is permanently ejected at *t* = 722 fs, as shown in Table 1.

This calculated flow in the charge density is consistent with the general principle of the Ln(Cp)₃ photodissociation mechanism described earlier. The chemistry begins with a ligand radical, created through the LMCT transition. The radical then cracks and a stable, closed-shell molecule is ejected. The retained radical fragment receives an electron back from the metal through a metal-to-ligand charge transfer (MLCT) process, forming an anion in a stable or at least metastable complex.

Tris(tetramethylcyclopentadienyl)lanthanide Precursors. PI-TOF Mass Spectra of Tb(TMCp)₃ and Gd(TMCp)₃. The tris(tetramethylcyclopentadienyl)lanthanide MOCVD precursors, Ln(TMCp)₃, have more favorable volatility than Ln(Cp)₃ and therefore were also investigated. In Figure 7 the PI-TOF mass spectrum of Tb(TMCp)₃ with photolysis at 430 nm

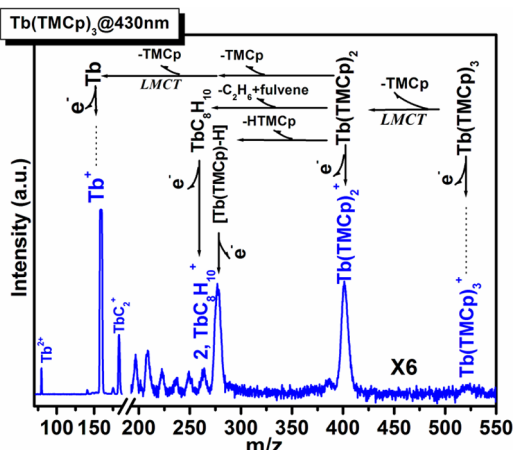


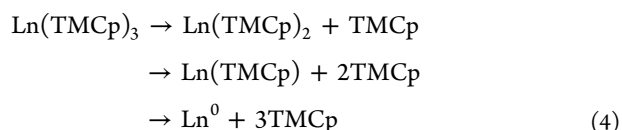
Figure 7. PI-TOF mass spectrum of Tb(TMCp)₃ with photolysis at 430 nm. Tb²⁺, Tb⁺, and TbC₂⁺ ions are observed as the most prominent fragments in the low mass range and Tb(TMCp)₃⁺, Tb(TMCp)₂⁺, and [Tb(TMCp) – H]⁺ ions in the high mass range.

nm is shown. As in the mass spectra of Ln(Cp)₃ discussed earlier, the dominant features are Tb²⁺, Tb⁺, and TbC₂⁺ fragments. Some heavier fragments, such as Tb(TMCp)₃⁺ and Tb(TMCp)₂⁺, are also observed, analogous to the Ln(Cp)₃⁺ and Ln(Cp)₂⁺ fragments observed in the mass spectra of Ln(Cp)₃. In contrast, however, no signal for Tb(TMCp)⁺ at *m/z* 318 amu is found; instead, a strong feature appears at *m/z* 317 amu, which we assign to [Tb(TMCp) – H]⁺, where the “–H” should be read a “minus H”.

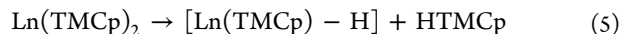
Between the [Tb(TMCp) – H]⁺ and TbC₂⁺ fragments there are several small features, expanded in the left panel of Figure 8, which provide evidence for the mechanism of ligand cracking, which leads to TbC_n⁺ products. In the lower panel, the same spectral region is shown for photoexcitation at 266 nm, which provides better resolution because of the better laser beam spatial profile. There are seven groups of features that are labeled as 1–7 and the peaks in each group are labeled as *n*, *n'*, and *n''* (*n* = 1–7), respectively. Feature 1 corresponds to [Tb(TMCp) – H]⁺. The loss of one H₂ molecule from feature 1 gives rise to feature 1', assigned as [Tb(TMCp) – 3H]⁺, and loss of another H₂ molecule from 1' produces fragment 1'', assigned as [Tb(TMCp) – SH]⁺. Similarly, as will be discussed below, the other fragments, *n*, *n'*, and *n''* are related to each other through the loss of H₂ molecules.

Under similar conditions, the mass spectrum of Gd(TMCp)₃, shows great similarity to the Tb(TMCp)₃ spectra. The dominant features observed are Gd(TMCp)₃⁺, Gd(TMCp)₂⁺, [Gd(TMCp) – H]⁺, GdC₂⁺, and Gd⁺ fragments (see the Supporting Information). The spectral region with *m/z* falling between [Gd(TMCp) – H]⁺ and GdC₂⁺ is expanded and shown in Figure 8, with features labeled with 1–7, in analogy to the Tb spectrum. The labels in Figure 8 correspond to the component with the heaviest of the isotopes of gadolinium, Gd-160.

Photofragmentation Mechanism of Ln(TMCp)₃. The mass spectra suggest the dominant photofragmentation pathway



with successive steps mediated by excitation to the repulsive wall of the LMCT state. This is very similar to the mechanism proposed for several other organic lanthanide complexes,^{10,20} including Ln(Cp)₃ above. In a competing mechanism



where the ejected TMCp radical extracts one hydrogen from the ligand which remains bound, thus leaving as the closed-shell molecule, HTMCp. The proposed mechanism whereby the [Ln(TMCp) – H] = Ln(C₉H₁₂) is formed is given in the top line of Scheme 2. The corresponding cation is labeled as feature 1 in Figure 8. The structure shown for feature 1 in Scheme 2 is calculated to be the lowest energy structure of several feasible candidates. The minimum electronic energies for the proposed structures and for the alternative structures are given in the Supporting Information. Feature 1*i* has a slightly higher energy than feature 1 and is thought to be an intermediate, leading to features 1' and 3 as illustrated in Scheme 3. Chirik et al.³⁵ have reported a “tuck-in” structure analogous to that proposed for feature 1 as an intermediate in H/D exchange in bis-

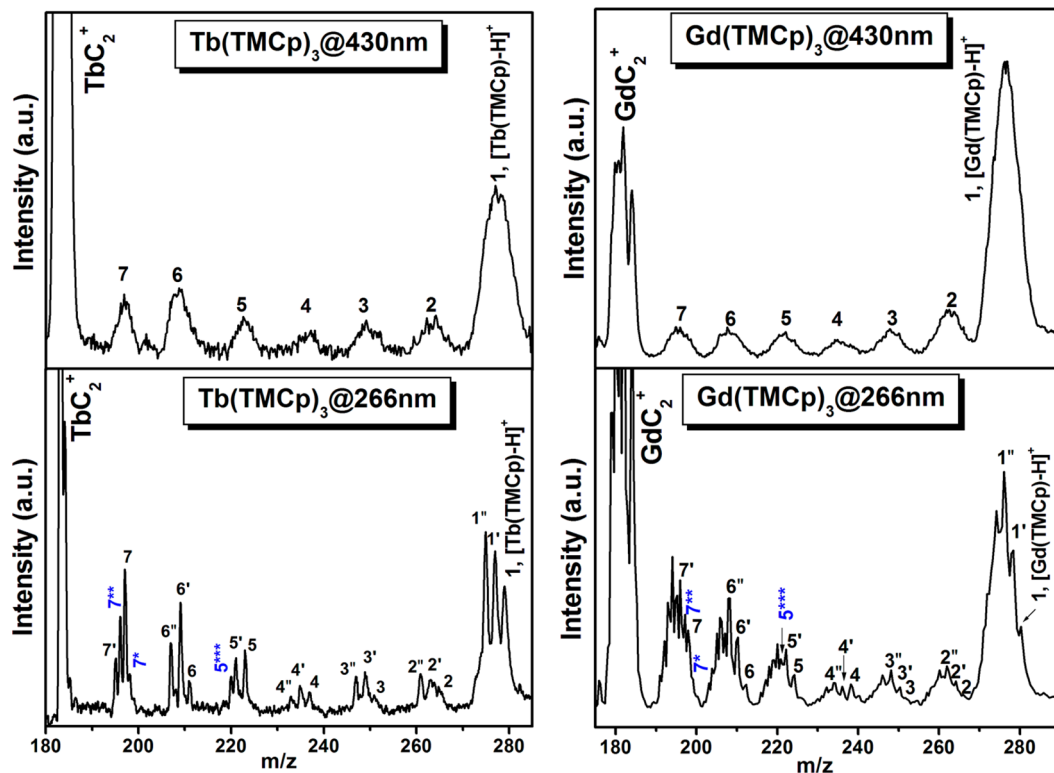
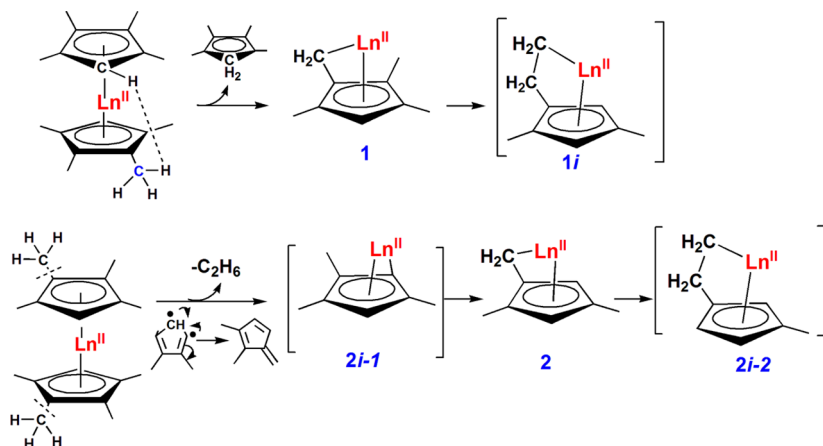


Figure 8. PI-TOF mass spectrum of $\text{Tb}(\text{TMCp})_3$ (left) and $\text{Gd}(\text{TMCp})_3$ (right) precursors with photolysis at 266 and 430 nm in the mass range between $[\text{Ln}(\text{TMCp}) - \text{H}]^+$ and LnC_2^+ fragments.

Scheme 2. Proposed Mechanism for $\text{Ln}(\text{TMCp})_2$ to $\text{Ln}[(\text{TMCp}) - \text{H}]$ and $\text{Ln}[(\text{TMCp}) - \text{CH}_3]^+$



^aThe oxidation state of the Ln ions is specified assuming the entire structure is neutral in charge. The structures in brackets, labeled **1i** and **2i**, are calculated as slightly less stable geometries than the structures labeled as **1** and **2** but are likely intermediates for the next reaction step.

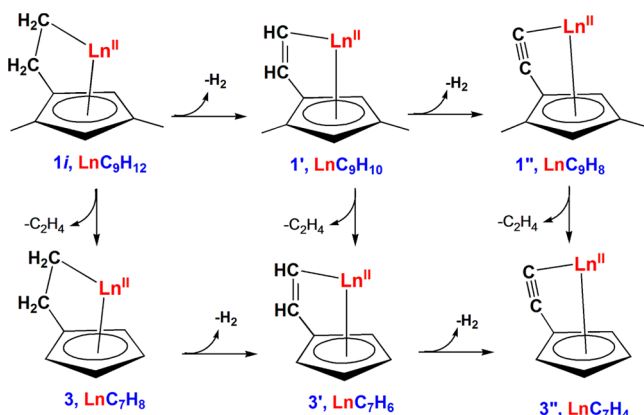
(pentamethylcyclopentadienyl)zirconium dihydride. Marks^{36,37} also reported a similar tuck-in structure for a Ti-based catalyst for ethylene and propylene polymerization.

Feature **2** in Figures 8 corresponds to $[\text{Ln}(\text{TMCp} - \text{CH}_3)]^+$ or $\text{Ln}(\text{C}_8\text{H}_{10})^+$, wherein the ligand bound to the metal is equivalent to TMCp “minus” a methyl group. It is unlikely that feature **2** derives directly from feature **1**, as this would require elimination of the open-shell fragment, CH_2 . It is suggested that a more probable mechanism is that, starting with the bis complex, an ejected TMCp radical extracts a methyl group from the ligand which remains bound, thus departing as the closed-shell molecule, pentamethylcyclopentadiene (136 amu, not observed in the PI-TOF spectrum), or, if both rings lose

methyl groups, departing as ethane C_2H_6 plus dimethylfulvene (30 + 106 amu, weakly observed), as illustrated in the second line of Scheme 2. Then the structure for feature **2** given in Scheme 2 is thought to be formed through an intermediate designated as **2i-1**, which is calculated to be slightly higher in energy than feature **2**.

The features labeled **1'** and **1''** in the mass spectra arise from feature **1** through sequential loss of H_2 (Scheme 3), as do **2'** and **2''** from feature **2**. Scheme 3 also shows how feature **3** may be formed from feature **1** with loss of ethene, C_2H_4 , together with the origin of **3'** and **3''** from **3** through sequential loss of H_2 . Scheme 4 shows how feature **6** may be formed from feature **4**, feature **4** from feature **2**, feature **7** from feature **5**, and feature

Scheme 3. Proposed Mechanism for Feature 1, $\text{Ln}(\text{TMCp}) - \text{H}$, to Feature 3'', LnC_7H_4^*



*The oxidation state of the Ln ions is specified assuming the entire structure is neutral in charge.

5 from feature 3, all with elimination of closed-shell molecules, ethene (C_2H_4) or acetylene (C_2H_2). The features labeled n' and n'' , as mentioned above, derive from n with sequential loss of H_2 . There are alternative connecting pathways that are illustrated in these schemes. For example, $1 \rightarrow 3 + \text{C}_2\text{H}_4 \rightarrow 3' + \text{H}_2 + \text{C}_2\text{H}_4$ might also be accomplished by $1 \rightarrow 1' + \text{H}_2 \rightarrow 3' + \text{C}_2\text{H}_4 + \text{H}_2$. That is, the order of the elimination steps for H_2 vs C_2H_4 is not known, and in fact, both may be active. The structures we propose for features 1–7, including those from H_2 elimination (e.g., $1'$ and $1''$), correspond to the result of DFT geometry optimization and the corresponding energies are given in the Supporting Information.

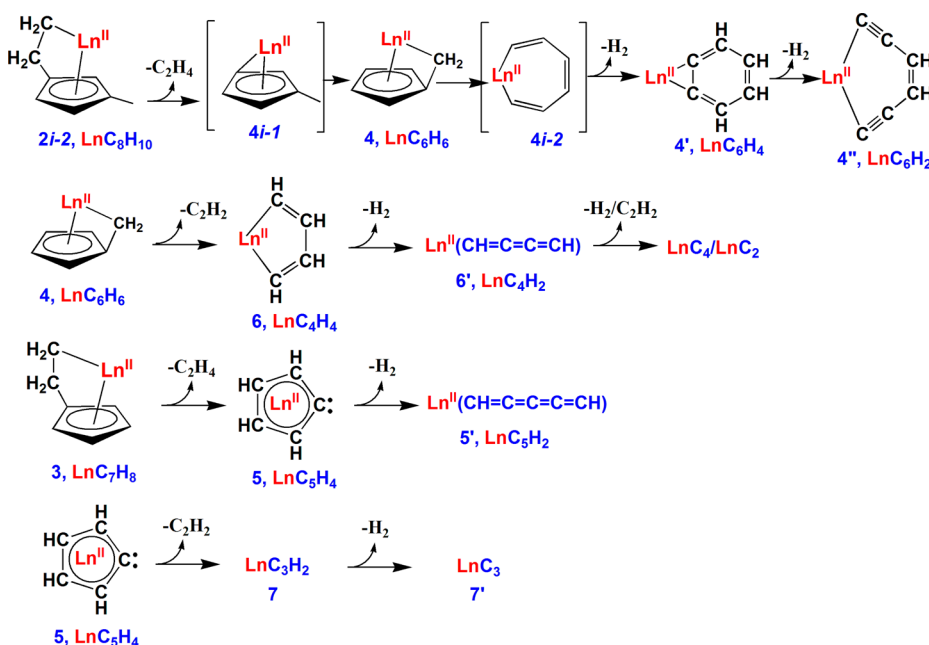
In general, the overall mechanism described above is dominated by species with even numbers of hydrogens. Starting with $\text{Ln}(\text{TMCp} - \text{H}) = \text{Ln}(\text{C}_9\text{H}_{12})$ or $\text{Ln}(\text{TMCp} - \text{CH}_3) = \text{Ln}(\text{C}_8\text{H}_{10})$, successive elimination of closed-shell

C_2H_{2n} and H_2 results in products which still have even numbers of hydrogens, since $2n$ is always an even number. To explain the appearance of some minor products with odd numbers of hydrogens (labeled in Figure 8 as $7^* = \text{LnC}_3\text{H}_3$, $7^{**} = \text{LnC}_3\text{H}_5$, $5^{***} = \text{LnC}_5\text{H}_5$, etc.), we invoke a chemistry that begins with $\text{Ln}(\text{TMCp}) = \text{Ln}(\text{C}_9\text{H}_{13})$, as illustrated in Scheme 5. The $\text{Ln}(\text{TMCp})$ produced as illustrated in eq 4 may not itself be highly stable and is not strongly observed in the mass spectra. However, it can sequentially lose two-carbon (C_2H_{2n}) and H_2 fragments to produce the observed minor features $2^* - 6^*$, plus relatively stronger features LnC_3H_3 (7^*), LnC_3H_5 (7^{**}), and LnC_5H_5 (5^{***}), as indicated in Scheme 5. These metal-containing fragments with odd numbers of hydrogens are generally minor products, but parallel chemistry may be easily observed in the fragmentation of the TMCp radical.

Similar fragments arise from bare TMCp , with dominant features at 105 (C_8H_9), 91 (C_7H_7), 77 (C_6H_5), 65 (C_5H_5), 63 (C_5H_3), 51 (C_4H_3), 39 (C_3H_3), and 37 (C_3H) amu in the low mass range of the mass spectrum of $\text{Gd}(\text{TMCp})_3$. A comparison of the TMCp mass spectral fragmentation with the purported $\text{Ln}(\text{TMCp})$ fragmentation pattern is given in the Supporting Information. Thus, we propose parallel chemistry for the $\text{Ln}(\text{TMCp})$ fragment illustrated in Scheme 5, where the photofragmentation proceeds from $\text{Ln}(\text{TMCp}) \rightarrow 2^* \rightarrow 4^* \rightarrow 6^*$ and $\text{Ln}(\text{TMCp}) \rightarrow 3^* \rightarrow 5^* \rightarrow 7^* \rightarrow 7^{**}$ or $3^* \rightarrow 5^{**} \rightarrow 5^{***}$ through two-carbon (C_2H_{2n}) or H_2 elimination, as discussed above.

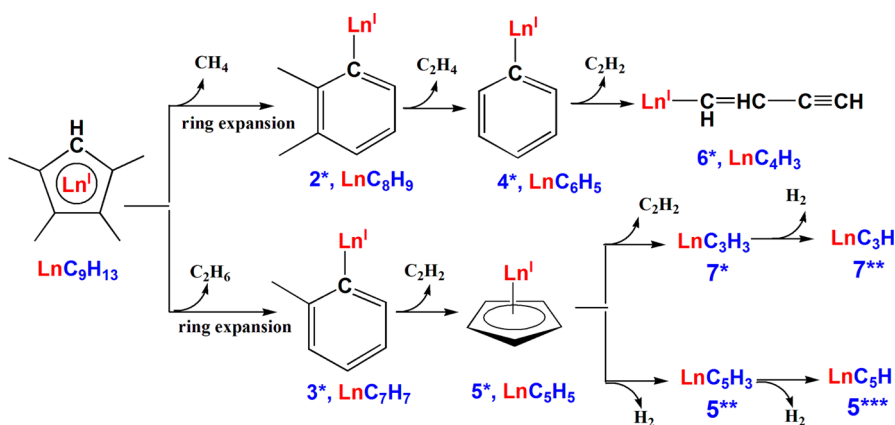
The photofragmentation of $\text{Ln}(\text{TMCp})_3$ was not simulated by TDESMO. However, evidence for the mechanism suggested here lies in the good correlation between fragments observed in the mass spectrum and those proposed in the mechanism. There are also many literature reports that bear resemblance to individual steps and structures that we propose. For example, in the first step of Scheme 2, feasibility of hydrogen migration from one Cp ring to the second ring is supported by the widely reported mobility of the ring hydrogen on Cp^{38} and by the

Scheme 4. Photofragmentation Mechanism from Feature 2 to Feature 7''*



*The oxidation state of the Ln ions is specified assuming the entire structure is neutral in charge.

Scheme 5. Photofragmentation Mechanism Starting from $\text{Ln}(\text{TMCP}) = \text{Ln}(\text{C}_9\text{H}_{13})$, Yielding Fragments with Odd Numbers of Hydrogens^a



^aThe oxidation state of the Ln ions is specified assuming the entire structure is neutral in charge.

specific example of $\text{Cp}_2\text{TiR}_2 \rightarrow [\text{Cp}-\text{H}]\text{CpTiR} + \text{RH}$ reported by Erskine et al.³⁹ Analogous to the lower line in Scheme 2, Moskalev et al.⁴⁰ reported formation of fulvene from the $\text{Cp} + \text{CH}_3$ reaction and Jackson et al.⁴¹ reported tetramethylfulvene formation from pentamethylcyclopentadienyl (PMCP) lanthanides by the reaction between several lanthanides, Ln^+ , and pentamethylcyclopentadiene (HPMCp). In that work, the lability of methyl groups on Cp rings, again relevant to line 2 of Scheme 2, was illustrated in the formation with nearly equal abundance of the complexes formed by H elimination (i.e. $\text{Ln}(\text{PMCP} - \text{H})$) and CH_3 elimination (i.e. $\text{Ln}(\text{PMCP} - \text{CH}_3)$).

Elimination of C_2H_{2n} fragments is a common theme in the reaction of metal ions with ring systems in the literature.⁴² The formation of the fragments labeled as $n = 3-7$ in Figure 8 and Schemes 3 and 4 are proposed to arise from elimination of two-carbon fragments from larger fragments labeled as $n - 2$, e.g., **1** \rightarrow **3** + C_2H_4 , **3** \rightarrow **5** + C_2H_4 , **5** \rightarrow **7** + C_2H_2 , **2** \rightarrow **4** + C_2H_4 , and **4** \rightarrow **6** + C_2H_2 . Dehydrogenation, invoked above in the formation of n' and n'' from n , is also commonly observed.⁴³

From the feature **4** \rightarrow **4'**, through the intermediate **4i**, H_2 elimination creates an aromatic structure in the six-membered ring (**4'**, LnC_6H_4^+). Reported gas-phase photodissociation of $\text{Ln}-\text{benzene}$ was proposed to yield this same dehydrogenation product ion, LnC_6H_4^+ .⁴⁴ In the proposed structure for feature **4i**, the lanthanide is inserted into the ring. A similar insertion was reported in previous work by Jarrold et al.,⁴⁵ where the lanthanum ion was inserted into a carbon ring when La^+ reacted with a carbon cluster by annealing. Insertion of a Ta^+ ion into a C_6H_6 ring was proposed to yield a similar structure, e.g. metallacycloheptatriene, in the photodissociation of $\text{Ta}^+ - \text{C}_6\text{H}_6$.⁴⁶ Feature **6** (LnC_4H_4) is also a well-established structure,⁴⁷ presented as a metallacyclopentadiene, $\text{Ln}^{2+}-(\eta^2-\text{CH}=\text{CH}-\text{CH}=\text{CH}^-)$.

The ring expansion of Scheme 5, which produces phenyl rings (features **2*** and **3***) from methyl-substituted cyclopentadienyls, is commonly invoked in soot chemistry, where methyl-substituted cyclopentadienyls are thought to be intermediates in the formation of polyaromatic hydrocarbons.^{40,48} Photodissociation of the phenyl radical was reported with a channel for C_2H_2 elimination⁴⁹ with cracking of C_6H_5 (77 amu) to yield C_4H_3 (51 amu) and C_2H_2 (26 amu),

identical with the chemistry from feature **4*** to **6*** invoked in the last step of the top line of Scheme 5.

The proposed photofragmentation mechanism for $\text{Ln}(\text{TMCP})_3$ in the gas phase as given in Schemes 2–5 is evidenced by the TOF-MS results and is strongly supported by DFT calculations of stable intermediate geometries as well as by reports of similar fragmentation phenomena in the literature.

The results and method described for this work are expected to apply to other lanthanide metal–organics. Even in cases where the molecules are too large for full TDESMO simulation of the reaction, the coupling of experimental measurements with computational geometry optimizations of intermediates can lead to a mostly unambiguous deduction of the mechanism. The mass spectrum, when properly optimized, can provide the masses of all of the stable intermediates. Once the masses are known, computational geometry optimization provides the identities of the most stable structures associated with those masses. As a check on that identification, one should be able to show, as in this instance, that the intermediate structures provide a chemically reasonable path leading step by step from the starting reactant to final products. In fact, in the current study, once the intermediates were identified, there was usually little uncertainty in the mechanistic path. There are few other methods whereby such a complex set of photochemical reactions can be so completely characterized.

CONCLUSION

Mechanisms for the unimolecular gas-phase laser-photo-dissociation reactions of lanthanide cyclopentadienyl (Cp) and tetramethylcyclopentadienyl (TMCP) complexes are proposed, on the basis of photoionization time-of-flight mass spectrometry measurements and computational simulations. Photodissociation is shown to branch between two reaction pathways: ligand ejection and ligand cracking within the metal–ligand complex. The cracking pathway leads to the production of lanthanide carbides, which could be a significant source of contamination for CVD-based production of high-purity thin films of metals or metal oxides.

DFT methods of time-dependent excited-state molecular dynamics are shown to be suitable for modeling photo-dissociation of large lanthanide-based complexes and provide valuable insight into the reaction mechanisms. Furthermore, our previously stated hypothesis regarding the central role of

charge transfer (LMCT and MLCT) in the photochemistry of the complex (for both reaction pathways) is strongly supported in the electronic structure calculations. Partial charge density maps of the initial and final-state molecular orbitals involved in the excitation clearly illustrate ligand cracking chemistry that results directly from ligand to metal charge transfer and, further, illustrates the subsequent stabilization of the metal-containing fragment by back-transfer of charge from the metal to the retained portion of the cracked ligand.

The cracking chemistry of the simple cyclopentadienyls, $\text{Ln}(\text{Cp})_3$, is dominated by the commonly observed disproportionation of the Cp radical into C_2H_2 and C_3H_3 fragments. The mobility of the methyl groups leads to a far richer chemistry in $\text{Ln}(\text{TMCp})_3$, where several tuck-in complexes and products of Cp ring expansion are revealed as intermediates. This project illustrates the great utility of PI-TOF-MS, coupled with straightforward computational methods, for deducing very complex photochemical mechanisms in metal–organic complexes. Furthermore, the results strongly suggest a hypothesis that, in many instances, the efficacy of metal ions in catalysis of organic reactions is strongly correlated to their ability to act as a reservoir, as both a sink and source of electrons, during the course of the reaction.

ASSOCIATED CONTENT

Supporting Information

Figures and tables giving PI-TOF mass spectra of $\text{La}(\text{Cp})_3$, $\text{Pr}(\text{Cp})_3$, $\text{Gd}(\text{Cp})_3$, $\text{Gd}(\text{TMCp})_3$, and $\text{Tb}(\text{TMCp})_3$ and proposed molecular structures and energies for intermediates in the mechanistic scheme for $\text{Ln}(\text{TMCp})_3$. This material is available free of charge via the Internet at <http://pubs.acs.org>.

AUTHOR INFORMATION

Corresponding Authors

*E-mail for Q.M.: Qingguo.Meng@usd.edu.

*E-mail for M.T.B.: Mary.Berry@usd.edu.

Notes

The authors declare no competing financial interest.

ACKNOWLEDGMENTS

This research was supported by the South Dakota Governor's Office of Economic Development and NSF award EPS-0903804. D.K. acknowledges computational resources provided by the DOE, BES-Chemical Sciences, NERSC Contract No. DE-AC02-05CH11231, allocation Award 86185 "Computational Modeling of Photocatalysis and Photoinduced Charge Transfer Dynamics on Surfaces". The authors acknowledge computational resources of the USD High Performance Computational Facilities cosponsored by the South Dakota iDeA Network of Biomedical Research Excellence NIH 2 P20RR016479 and operated by Douglas Jennewein.

REFERENCES

- (1) Wang, X.; Dong, L.; Zhang, J.; Liu, Y.; Ye, P. D.; Gordon, R. G. *Nano Lett.* **2013**, *13* (2), 594–599.
- (2) Magadur, G.; Bouanis, F.; Norman, E.; Guillot, R.; Lauret, J.; Huc, V.; Cojocaru, C.; Mallah, T. *Chem. Commun.* **2012**, *48*, 9071–9073.
- (3) Bünzli, J.; Piguet, C. *Chem. Soc. Rev.* **2005**, *34*, 1048–1077.
- (4) Norton, D. P.; Goyal, A.; Budai, J. D.; Christen, D. K.; Kroeger, D. M.; Specht, E. D.; He, Q.; Saffian, B.; Paranthaman, M.; Klabunde, C. E.; Lee, D. F.; Sales, B. C.; List, F. A. *Science* **1996**, *274* (5288), 755–757.
- (5) Hong, M.; Kwo, J.; Kortan, A. R.; Mannaerts, J. P.; Sergent, A. M. *Science* **1999**, *283*, 1897–1900.
- (6) Schlam, D. G.; Haeni, J. H. *MRS Bull.* **2002**, *27* (3), 198–204.
- (7) Gaskell, J. M.; Przybylak, S.; Jones, A. C.; Aspinall, H. C.; Chalker, P. R.; Black, K.; Potter, R. J.; Taechakumput, P.; Taylor, S. *Chem. Mater.* **2007**, *19*, 4796–4803.
- (8) Päiväsaari, J.; Niinistö, J.; Arstila, K.; Kukli, K.; Putkonen, M.; Niinistö, L. *Chem. Vap. Deposition* **2005**, *11*, 415–419.
- (9) Muraoka, P. T.; Byun, D.; Zink, J. I. *J. Am. Chem. Soc.* **2000**, *122* (6), 1227–1228.
- (10) Meng, Q. G.; Witte, R. J.; May, P. S.; Berry, M. T. *Chem. Mater.* **2009**, *21* (24), 5801–5808.
- (11) Nelson, B. N.; Caster, A. G.; Berry, M. T. *Chem. Phys. Lett.* **2004**, *396*, 256–260.
- (12) Meng, Q. G.; Witte, R. J.; Gong, Y. J.; Day, E. L.; Chen, J. C.; May, P. S.; Berry, M. T. *Chem. Mater.* **2010**, *22* (22), 6056–6064.
- (13) Rutkowski, P. X.; Zink, J. I. *Inorg. Chem.* **2009**, *48* (4), 1655–1660.
- (14) Ow, F. P.; Djurovich, P. I.; Thompson, M. E.; Zink, J. I. *Inorg. Chem.* **2008**, *47* (7), 2389–2395.
- (15) Ow, F. P.; Berry, M. T.; May, P. S.; Zink, J. I. *J. Phys. Chem. A* **2007**, *111*, 4144–4149.
- (16) Chen, J. C.; Meng, Q. G.; May, P. S.; Berry, M. T.; Kilin, D. *Mol. Phys.* **2013**, *112*, 508–517.
- (17) Kohn, W.; Sham, L. *Phys. Rev. A* **1965**, *140*, 1133–1138.
- (18) Perdew, J. P.; Burke, K.; Ernzerhof, M. *Phys. Rev. Lett.* **1996**, *77*, 3865–3868.
- (19) Vanderbilt, D. *Phys. Rev. B* **1990**, *41*, 7892–7895.
- (20) Ow, F. P.; Berry, M. T.; May, P. S.; Zink, J. I. *J. Phys. Chem. A* **2006**, *110*, 7751–7754.
- (21) Bacskay, G. B.; Mackie, J. C. *Phys. Chem. Chem. Phys.* **2001**, *3*, 2467–2473.
- (22) Roy, K.; Horn, C.; Frank, P.; Slutsky, V. G.; Just, T. *Twenty-Seventh Symposium (International) on Combustion*; The Combustion Institute: Pittsburgh, PA, 1998; pp 329–336.
- (23) Kern, R. D.; Zhang, Q.; Yao, J.; Jursic, B. S.; Tranter, R. S.; Greybill, M. A.; Kiefer, J. H. *Twenty-Seventh Symposium (International) on Combustion*; The Combustion Institute: Pittsburgh, PA, 1998; pp 143–150.
- (24) Becke, A. D. *J. Chem. Phys.* **1993**, *98*, 5648–5652.
- (25) Moskaleva, L. V.; Lin, M. C. *J. Comput. Chem.* **2000**, *21* (6), 415–425.
- (26) (a) Ren, J.; Zhou, G.; Hu, Y.; Zhang, D. W. *Appl. Surf. Sci.* **2009**, *255*, 7136–7141. (b) Ren, J.; Cui, C.; Zhou, G.; Liu, Y.; Hu, Y.; Wang, B. *Thin Solid Films* **2011**, *519*, 3716–3721.
- (27) Muraoka, P. T.; Byun, D.; Zink, J. I. *J. Phys. Chem. A* **2001**, *105*, 8665–8671.
- (28) Hinrichs, R. Z.; Schröden, J. J.; Davis, H. F. *J. Phys. Chem. A* **2008**, *112*, 3010–3019.
- (29) (a) Suzuki, S.; Torisu, H.; Kubota, H.; Wakabayashi, T.; Shiromaru, H.; Achiba, Y. *Int. J. Mass Spectrom. Ion Processes* **1994**, *138*, 297–306. (b) Gingerich, K. A. *J. Less-Common Metals* **1985**, *110*, 41–51.
- (30) Gibson, J. K. *J. Vac. Sci. Technol. A* **1997**, *15*, 2107–2118.
- (31) Car, R.; Parrinello, M. *Phys. Rev. Lett.* **1985**, *55*, 2471–2474.
- (32) Meng, Q. G.; May, P. S.; Berry, M. T.; Kilin, D. *Int. J. Quantum Chem.* **2012**, *112* (24), 3896–3903.
- (33) (a) Allen, L.; Eberly, J. H. *Optical resonance and two-level atoms*; Wiley: New York, 1975. (b) Carmichael, H. *Statistical Methods in Quantum Optics 2: Non-Classical Fields*; Springer: Berlin, 2007.
- (34) Tully, J. C. *J. Chem. Phys.* **1990**, *93* (2), 1061–1071.
- (35) Chirik, P. J.; Day, M. W.; Bercaw, J. E. *Organometallics* **1999**, *18* (10), 1873–1881.
- (36) Chen, Y. X.; Marks, T. J. *Organometallics* **1997**, *16* (16), 3649–3657.
- (37) Schock, L. E.; Marks, T. J. *J. Am. Chem. Soc.* **1988**, *110*, 7701–7715.
- (38) Razuvayev, G. A.; Marin, V. P.; Andriznov, Y. A. *J. Organomet. Chem.* **1979**, *174*, 67–75.

- (39) Erskine, G. J.; Hartgerink, J.; Weinberg, E. L.; McCowan, J. D. *J. Organomet. Chem.* **1979**, *170*, 51–61.
- (40) Moskaleva, L. V.; Mebel, A. M.; Lin, M. C. *Twenty-Sixth Symposium (International) on Combustion*; The Combustion Institute: Pittsburgh, PA, 1998; pp 521–526.
- (41) Jackson, G. P.; Gibson, J. K.; Duchworth, D. C. *Int. J. Mass Spectrom.* **2002**, *220*, 419–441.
- (42) Huang, Y.; Hill, Y. D.; Sodupe, M.; Bauschlicher, C. W.; Freiser, B. S. *Inorg. Chem.* **1991**, *30*, 3822–3829.
- (43) (a) Ranasinghe, Y. A.; MacMahon, T. J.; Freiser, B. S. *J. Am. Chem. Soc.* **1992**, *114*, 9112–9118. (b) Parent, D. C.; McElvany, S. W. *J. Am. Chem. Soc.* **1989**, *111*, 2393–2401.
- (44) (a) Gibson, J. K. *J. Phys. Chem.* **1996**, *100*, 15688–15694. (b) Pope, R. M.; Van Orden, S. L.; Cooper, B. T.; Buckner, S. W. *Organometallics* **1992**, *11*, 2001–2003. (c) Burkner, S. W.; Pope, R. M. *Int. J. Mass Spectrom.* **1999**, *182*|*183*, 197–201.
- (45) Clemmer, D. E.; Shelimov, K. B.; Jarrold, M. F. *J. Am. Chem. Soc.* **1994**, *116*, 5971–5972.
- (46) Lee, H. F.; Lin, F. W.; Yeh, C. S. *J. Mass Spectrom.* **2001**, *36*, 493–499.
- (47) Wesendrup, R.; Schwarz, H. *Organometallics* **1997**, *16*, 461–466.
- (48) (a) Scheer, A. M.; Mukarakate, C.; Robichaud, D. J.; Ellison, G. B.; Nimlos, M. R. *J. Phys. Chem. A* **2010**, *114* (34), 9043–9056. (b) Fascella, S.; Cavallotti, C.; Rota, R.; Carra, S. *J. Phys. Chem. A* **2005**, *109*, 7546–7557.
- (49) Negru, B.; Goncher, S. J.; Brunsvold, A. L.; Just, G. M. P.; Park, D.; Neumark, D. M. *J. Chem. Phys.* **2010**, *133*, 074302.